Impedance-Based Analysis of DC-Link Voltage Dynamics in Voltage-Source Converters

Dapeng Lu, *Student Member, IEEE*, Xiongfei Wang, *Senior Member, IEEE*, and Frede Blaabjerg, *Fellow, IEEE*

***Abstract*—This paper addresses the stability issues caused by the dc-link voltage control of grid-connected voltage-source converters. An analytical impedance model is developed first for capturing the interactions between the dc-link voltage control and ac current control of converters, which enables to identify different stability impacts of the dc-link voltage control in the rectifier and inverter operation modes of converters. The impedance model is further transformed from the dq-frame to the $\alpha\beta$-frame, which allows characterizing the frequency-coupling effects of the dc-link voltage control dynamics. The impedance-based analysis reveals that the dc-link voltage control may cause low-frequency oscillations in the rectifier mode and high-frequency oscillations in the inverter mode. Case studies on the rectifier and inverter operation modes are presented, and subsequently validated by using time-domain simulations and experimental tests. The close correlations between the measured results and theoretical analysis demonstrate the effectiveness of the impedance model and stability analysis.**

***Index Terms*—DC-link voltage control, frequency-coupling, impedance model, stability, voltage-source converters (VSCs).**

I. Introduction

VOLTAGE-SOURCE converters (VSCs) are increasingly used in power system applications for improving the energy efficiency and the power controllability [1], [2]. The stability of VSCs under the different grid conditions are attracting more and more attentions, due to their multiple-timescale dynamics contributed by the dc-link voltage control, the grid synchronization, and the current control loops [3]. The stability of current control with L-/LCL-filters has been well documented in the literature [4]–[6], which is found highly dependent on the time delay in the digital control system. The dynamic impact of the grid synchronization loop has also been discussed recently [7]–[9]. It is found that the frequency-coupling oscillations may be induced by the phase-locked loop (PLL) [9]. In contrast, only a few works have taken the dc-link voltage control into the stability analysis of grid-VSC interactions.

A general method of analyzing the dc-link voltage dynamics is to build a small-signal model of the VSC in the dq-frame, which enables to characterize the closed-loop control dynamics of the VSC [10]–[13]. Based on that, a reduced-order (RO) model including the dc-link dynamics is developed for the rectifier operation mode of VSCs with the unity power factor [14]. In the RO model, the stability of dc-link voltage control is determined by the d-axis control dynamics, and a single-input-single-output (SISO) model with a non-minimum-phase response is further developed. This non-minimum-phase characteristic is critical for the stability of the dc-link voltage control [15]. However, these models overlook the cross couplings between the d- and q-axes dynamics. Moreover, the ac-dc interactions, i.e., the interactions between the ac current control and the dc-link voltage control, are assumed to be negligible by intentionally separating the timescales of the control loops [13]. Consequently, the RO and SISO models can only predict the system dynamics in the low-frequency range, and will lose the accuracy in analyzing the high-frequency dynamics. Hence, the RO and SISO models are merely oriented for the controller design, which is incapable of revealing the effect of such ac–dc interactions on the system stability.

Two approaches have thus been developed recently to analyze the stability of the dc-link voltage control. In the first approach, the dynamics of VSCs are analogy to those of synchronous generators, where the dc-link dynamics are mapped to the dynamics of the rotor speed of synchronous generators [16]. Thus, the low-frequency oscillations caused by the dc-link voltage control can be predicted in a similar way to traditional synchronous-generator-based power systems [17], [18]. However, this virtual synchronous generator model limits the VSC dynamics to the timescale of the dc-link voltage control, which is around 100 ms [17]. Consequently, only the low-frequency responses of the VSC are modeled, whereas the ac current control dynamics are neglected, and thus, the impact of the ac current control on the dc-link voltage dynamics is not considered.

The second method of analyzing the dc-link dynamics is the impedance-based approach [18], [19], which utilizes the impedance concept to get the physical insight into the VSC dynamics. It is found that the dc-link voltage control may introduce a negative impedance, i.e., impedance with negative real part, at the VSC output impedance [3], [20]–[24], which tends to result in unexpected resonances near the fundamental frequency [3]. In [3], [20], the impedance model of the dc-link voltage control is formulated through the power balance, where only the d-d channel of the input admittance is affected by the dc-link voltage control. To improve the accuracy of the impedance model, the instantaneous power of the input L-filter is considered in the

Manuscript received December 8, 2017; revised April 30, 2018; accepted July 9, 2018. Date of publication August 19, 2018; date of current version February 20, 2019. This work was supported by Villum Fonden under the Villum Investigators Grant—Reliable Power Electronic based Power System. Recommended for publication by Associate Editor F. H. Khan. *(Corresponding author: Xiongfei Wang.)*

The authors are with the Department of Energy Technology, Aalborg University, Aalborg 9220, Denmark (e-mail: dap@et.aau.dk; xwa@et.aau.dk; fbl@et.aau.dk).

Color versions of one or more of the figures in this paper are available online at http://ieeexplore.ieee.org.

Digital Object Identifier 10.1109/TPEL.2018.2856745

0885-8993 © 2018 IEEE. Translations and content mining are permitted for academic research only. Personal use is also permitted, but republication/redistribution requires IEEE permission. See http://www.ieee.org/publications_standards/publications/rights/index.html for more information.

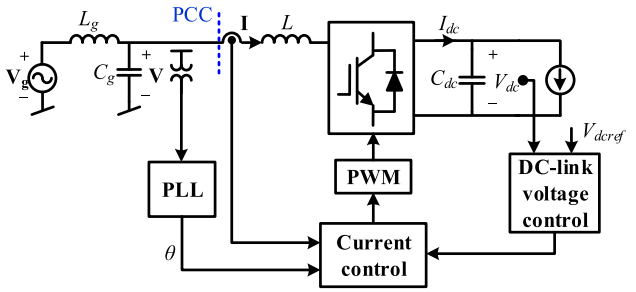

Fig. 1. Single-line circuit diagram and control system of a three-phase VSC.

power balance, and the stability of VSCs differs from the rectifier mode to the inverter mode [25]. However, the overlooked couplings between the *d*- and *q*-axes may give the inaccurate stability prediction [26]. Hence, the impedance matrix is used for the stability analysis [21], [23], which indicates that the negative impedance introduced by the dc-link voltage control is due to the constant power load behavior during the rectifier operation mode of VSCs. Nevertheless, the contributions of the VSC system parameters to the negative impedance derived in the dq-frame are not explicitly identified. The dynamic interactions between the dc-link voltage control and the ac current control are also overlooked, which affects the accuracy of the system impedance. Moreover, the frequency-coupling dynamics caused by the dc-link control is not characterized [9].

This paper thus presents a comprehensive analysis on the stability impact of the dc-link voltage control for grid-connected VSCs. Both the rectifier and inverter operation modes of VSCs are investigated. The interactions between the ac current control and the dc-link voltage control are characterized, which reveals that the critical value of the dc-link voltage controller gain differs from the inverter mode to the rectifier mode. Moreover, a parametric impedance model including the dc-link voltage control is developed for VSCs, which, differing from the existing dc-link dynamic analysis [14], [20], explicitly identifies the effects of VSC system parameters on the output negative impedance. The developed impedance model is further transformed from the dq-frame to the $\alpha\beta$-frame [9], and thus, the frequency-coupling effects of dc-link dynamics can be characterized. Simulation and experimental results are given to validate the effectiveness of the impedance model and the stability analysis.

II. Modeling of VSCs

A. System Description

Fig. 1 shows the diagram of a single-line circuit diagram of a three-phase VSC, where an input *L*-filter and an LC-type grid impedance are considered at the ac side. The dc-link is connected through a capacitor to a dc current source. The cascaded controllers are implemented in the dq-frame, where the dc-link voltage control generates the *d*-axis reference of the current control. Both the dc-link voltage control and the current control are realized with Proportional + Integral (PI) controllers. The voltage at the point of common coupling (PCC) is measured to synchronize the VSC with the grid by the PLL. The bandwidth

TABLE I
Main Circuit Parameters in a Three-phase VSC

Symbol	Electrical parameter	Value (p.u.)
V_g	Grid voltage (line to line)	173 V (1), 50 Hz (1)
V_{dc}	DC-link voltage	300 V (1.73)
P	Active power	1.5 kW (1)
Q	Reactive power	0 var (0)
L_g	Grid impedance (inductance)	5 mH (0.079)
C_g	Grid impedance (capacitance)	20 μF (7.98)
L	Input L-filter	3 mH (0.047)
C_{dc}	DC-link capacitor	500 μF (0.32)
f_s	Switching frequency	10 kHz (200)
T_s	Sampling time	100 μs (0.005)

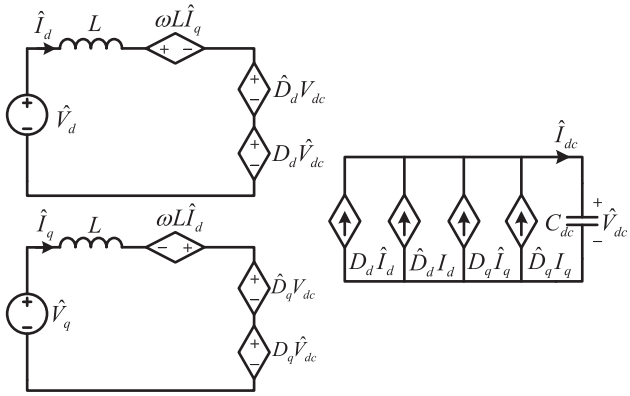

Fig. 2. Small-signal circuit of a VSC in the dq-frame.

of the PLL is intentionally designed as a low value in this paper, which allows neglecting the dynamic effects of the PLL in the stability analysis. Table I provides the main circuit parameters.

For clarity, "$\hat{\cdot}$" denotes the small-signal perturbation of a variable. Bold letters are used in this paper to denote space vectors in the dq-frame, e.g., $\mathbf{V} = [V_d\ V_q]^{\mathrm{T}}$ and $\mathbf{I} = [I_d\ I_q]^{\mathrm{T}}$ for the PCC voltage and input current, respectively, and transfer function matrices, e.g., $\hat{\mathbf{I}} = \mathbf{Y_{op}}\hat{\mathbf{V}}$, where $\mathbf{Y_{op}}$ is the open-loop input admittance. The corresponding elements of vectors and transfer function matrices are represented by italic letters, e.g., $[V_d, V_q]^{\mathrm{T}} \leftrightarrow \mathbf{V}$. A subscript "*d*", "*q*" is added for space vectors and transfer functions referred to the dq-frame and a subscript "α", "β" is added for space vectors and transfer function matrices referred to the $\alpha\beta$-frame. Complex space vectors and complex transfer function matrices are denoted with the subscript "dq" or "$\alpha\beta$" depending on their frames.

B. Small-Signal Model

Fig. 2 depicts the small-signal equivalent circuit of a VSC in the dq-frame, where the dc-link dynamics have been included. Then, combined with the control loops, the small-signal model can be represented by the block diagram of transfer function matrices, as shown in Fig. 3. In the plant of the VSC, $\mathbf{G_{p-dc}}$ is the transfer function matrix from the duty cycle vector to the dc-link voltage, $\mathbf{G_{p-ac}}$ is the transfer function matrix from the duty cycle vector to the input current vector and $\mathbf{Y_{op}}$ is the open-loop input admittance in the ac side. In the control part,

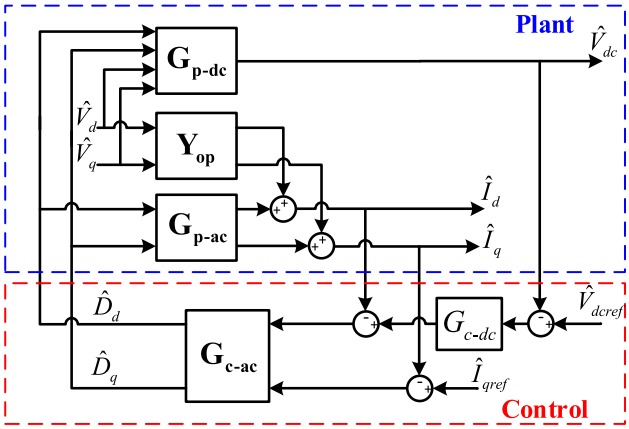

Fig. 3. Small-signal model of the VSC.

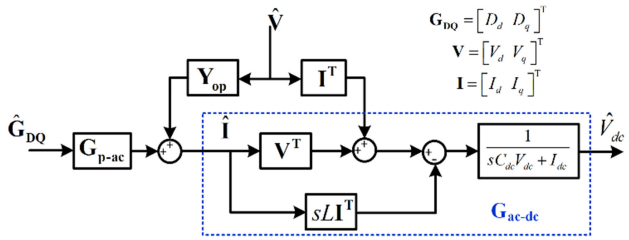

Fig. 4. Small-signal model of dc-link dynamics $\mathbf{G_{p-dc}}$.

$\mathbf{G_{c-ac}}$ is the current controller and $G_{\text{c-dc}}$ is the dc-link voltage controller. The expression of $\mathbf{G_{c-ac}}$ is

$$\mathbf{G_{c-ac}}=\begin{bmatrix}G_{\text{c-ac}} & 0\\ 0 & G_{\text{c-ac}}\end{bmatrix}=\begin{bmatrix}k_{pac}+k_{iac}/s & 0\\ 0 & k_{pac}+k_{iac}/s\end{bmatrix} \tag{1}$$

where G_{c-ac} is the current controller in d-and q-axes. k_{pac} and k_{iac} are the proportional gain and integral gain of the current PI controllers.

Since the plant is a two-input-three-output system from the control to outputs, three outputs are dependent and $\mathbf{G_{p-dc}}$ can be simplified as shown in Fig. 4, where $\mathbf{G_{ac-dc}}$ is the transfer function matrix from the input current vector to the dc-link voltage. Assuming the VSC is working with unity power factor, the expressions of $\mathbf{G_{ac-dc}}$, $\mathbf{G_{p-dc}}$ and $\mathbf{G_{p-ac}}$ are

$$\mathbf{G_{ac-dc}}=[G_d\ \ G_q]=\left[\frac{LI_d}{C_{\text{dc}}V_{\text{dc}}}\ \frac{-s+\frac{V_d}{LI_d}}{s+\frac{I_{\text{dc}}}{C_{\text{dc}}V_{\text{dc}}}}\ 0\right] \tag{2}$$

$$\mathbf{G_{p-dc}}=\mathbf{G_{ac-dc}}\mathbf{G_{p-ac}} \tag{3}$$

$$\mathbf{G_{p-ac}}=\begin{bmatrix}G_{dd} & G_{dq}\\ G_{qd} & G_{qq}\end{bmatrix}$$

$$=\begin{bmatrix}-\frac{V_{\text{dc}}}{L}\frac{s+\frac{I_{\text{dc}}}{C_{\text{dc}}V_{\text{dc}}}}{s^2+\omega_1^2+\frac{D_d^2+D_q^2}{LC_{\text{dc}}}} & -\frac{V_{\text{dc}}}{L}\frac{\omega_1}{s}\frac{s+\frac{I_{\text{dc}}}{C_{\text{dc}}V_{\text{dc}}}}{s^2+\omega_1^2+\frac{D_d^2+D_q^2}{LC_{\text{dc}}}}\\ \frac{D_qI_d+\omega_1C_{\text{dc}}V_{\text{dc}}}{LC_{\text{dc}}}\frac{1}{s^2+\omega_1^2+\frac{D_d^2+D_q^2}{LC_{\text{dc}}}} & -\frac{V_{\text{dc}}}{L}\frac{1}{s}\frac{s^2+\frac{D_d^2}{LC_{\text{dc}}}}{s^2+\omega_1^2+\frac{D_d^2+D_q^2}{LC_{\text{dc}}}}\end{bmatrix}. \tag{4}$$

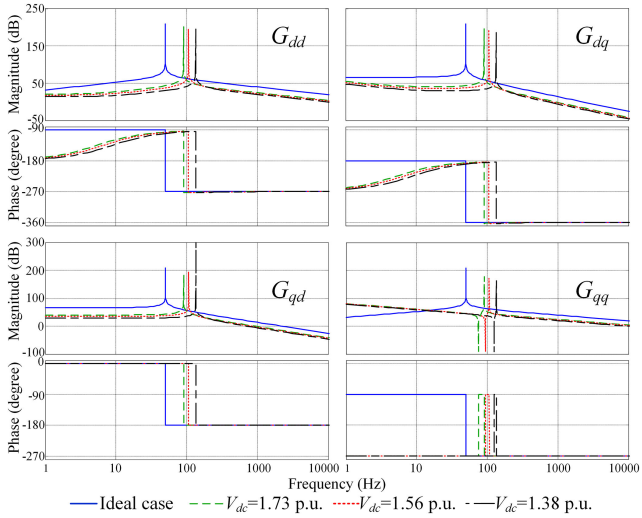

Fig. 5. Frequency response of four channels of L-filter plant and $\mathbf{G_{p-ac}}$ different dc-link voltage levels.

It is noted that $\mathbf{G_{ac-dc}}$ also agrees with the rule of the active power balance including the instantaneous power of the input L-filter in [25]. The linearization of the active power balance is given as follows, which shows the same result as given in (3)

$$\begin{aligned}\hat{P}&=V_d\hat{I}_d+V_q\hat{I}_q-\frac{L}{2}\frac{d(\hat{I}_d^2+\hat{I}_q^2)}{dt}\\&=\frac{C_{\text{dc}}}{2}\frac{d(\hat{V}_{\text{dc}}^2)}{dt}+\hat{V}_{\text{dc}}I_{\text{dc}}\\&\Rightarrow G_d=\frac{\hat{V}_{\text{dc}}}{\hat{I}_d}=\frac{-sLI_d+V_d}{sC_{\text{dc}}V_{\text{dc}}+I_{\text{dc}}}.\end{aligned} \tag{5}$$

From (5), it can be obtained that the pole in G_d, located at $-I_{\text{dc}}/C_{\text{dc}}V_{\text{dc}}$, is caused by the linearization of the energy stored in the dc-link capacitor. Moreover, the instantaneous power of the input L-filter introduces a zero at $-V_d/LI_d$, which is a right half plane (RHP) zero in the rectifier mode. It leads to the nonminimal-phase response of the dc-link dynamics.

Compared with the ac L-filter plant without dc-link, $\mathbf{G_{pL}}$, i.e., the plant of ac current control loop with the ideal dc voltage source, given as follows:

$$\mathbf{G_{pL}}=-\frac{V_{\text{dc}}}{L(s^2+\omega_1^2)}\begin{bmatrix}s & \omega_1\\ -\omega_1 & s\end{bmatrix} \tag{6}$$

both the poles and zeros in the elements of $\mathbf{G_{p-ac}}$ are affected by the ac-side and the dc-link parameters. It indicates that the dc-link has influences on the ac current control plant and the impacts depend on the grid voltage and load condition. With a low fundamental frequency and small passive filters, ω_1^2 is negligible and the resonant frequency is near the one proposed in the RO model [14]. However, in many applications, ω_1^2 is close to $\frac{D_d^2+D_q^2}{LC_{\text{dc}}}$, thus the RO model cannot adequately capture the system dynamics.

To investigate the detailed ac–dc interactions, Fig. 5 shows the frequency responses of the L-filter plant and $\mathbf{G_{p-ac}}$ with different operation points. The dc-link capacitor remains the

same for all cases. It can be seen that $\mathbf{G_{p-ac}}$ is close to the ideal *L*-filter plant when the dc-link voltage is much higher than the grid voltage. However, when decreasing the dc-link voltage, the frequency responses change significantly, where the resonant frequency moves towards a higher frequency range and the magnitude responses in the low-frequency range are different. It proves that the ac–dc interactions play an important role in the low dc-link voltage applications, where the current control plant cannot be overlooked.

III. DC-Link Voltage Control

In this section, the open-loop analysis of the dc-link voltage control is presented first, which varies from the rectifier mode to the inverter mode. A SISO model containing the ac–dc interactions for the dc-link voltage control is derived and the dominant poles and zeros in the system dynamics are discussed. Based on the open-loop analysis, the limitations of the dc-link voltage controller are obtained, which can be used to guarantee the closed-loop stability.

A. Open-Loop Analysis

The open-loop gain $\mathbf{T_o}$ of the dc-link voltage control can be derived as

$$\mathbf{T_o} = \mathbf{G_{ac-dc}}\mathbf{G_{cl}}\mathbf{G}^{\mathrm{T}}_{\mathbf{c-dc}} \tag{7}$$

where $\mathbf{G_{cl}}$ is the closed-loop gain of the current control, which is given by

$$\begin{aligned}\mathbf{G_{cl}} &= \begin{bmatrix} G_{cldd} & G_{cldq} \\ G_{clqd} & G_{clqq} \end{bmatrix} \\ &= \mathbf{G_{c-ac}}\mathbf{G_{del}}\mathbf{G_{p-ac}}(\mathbf{I} + \mathbf{G_{c-ac}}\mathbf{G_{del}}\mathbf{G_{p-ac}})^{-1}\end{aligned} \tag{8}$$

where $\mathbf{G_{c-dc}}$ is the vector form of the dc-link voltage controller. With the unity power factor operation, the *q*-axis current reference I_{qref} is equal to zero, and thus, $\mathbf{G_{c-dc}}$ can be rewritten as

$$\mathbf{G_{c-dc}} = \begin{bmatrix} G_{\mathrm{c-dc}} & 0 \end{bmatrix} \tag{9}$$

$\mathbf{G_{de1}}$ denotes the digital time delay effect, e.g., [28]

$$\mathbf{G_{del}} = \begin{bmatrix} G_{\mathrm{del}} & 0 \\ 0 & G_{\mathrm{del}} \end{bmatrix} = \begin{bmatrix} e^{-1.5T_s s} & 0 \\ 0 & e^{-1.5T_s s} \end{bmatrix}. \tag{10}$$

Substituting (3), (8), and (9) into (7) leads to

$$\mathbf{T_o} = G_{\mathrm{c-dc}} \underbrace{G_{cldd}}_{d-d\mathrm{channel}} G_d. \tag{11}$$

Obviously, only the *d-d* channel of the closed-loop current control G_{cldd} can affect the open-loop gain of the dc-link voltage, which also demonstrates that the *d-d* channel is the predominant element in the VSC with unity power factor. Yet, instead of a unity gain or a first-order system given in [20], [25], the *d-d* channel derived in this paper gives more insights into the ac-side dynamics, which contains not only the effect of the dc-link voltage dynamics on the ac side, but also the cross coupling between the *d*- and *q*-axes. Since the open loop zeros remain the same in the closed-loop gain, G_{cldd} can be rewritten as

$$G_{cldd} = G^{p}_{cldd}\left(s + \frac{I_{\mathrm{dc}}}{C_{\mathrm{dc}}V_{\mathrm{dc}}}\right) \tag{12}$$

where G^{p}_{cldd} represents the rest part except the zero. Substituting (12) into (11) yields

$$\begin{aligned}\mathbf{T_o} &= G_{c-\mathrm{dc}}G_{\mathrm{cldd}}G_d \\ &= G_{\mathrm{c-dc}}\underbrace{G^{p}_{\mathrm{cldd}}\left(s + \frac{I_{\mathrm{dc}}}{C_{\mathrm{dc}}V_{\mathrm{dc}}}\right)}_{G_{\mathrm{cldd}}}\underbrace{\frac{LI_d}{C_{\mathrm{dc}}V_{\mathrm{dc}}}\frac{-s + \frac{V_d}{LI_d}}{s + \frac{I_{\mathrm{dc}}}{C_{\mathrm{dc}}V_{\mathrm{dc}}}}}_{G_d}\end{aligned} \tag{13}$$

which describes that the pole located at $-I_{\mathrm{dc}}/C_{\mathrm{dc}}V_{\mathrm{dc}}$ in G_d can be cancelled by the zero in G_{cldd}. Hence, the dc controller design is independent of this pole, even in the inverter mode, where the pole located in the RHP would not introduce instability issues.

Fig. 6 shows the pole-zero map of G_{cldd} with the different active powers from the rectifier mode (2 per unit (p.u.), 1 p.u.) to the inverter mode (–1 p.u., –2 p.u.). A third-order Pade approximation is applied to G_{del}. By neglecting the poles and zeros above the Nyquist frequency, which has little influence on the system dynamics, it can be seen that one dominant pole and one zero exist in each case. The closed-loop zero is the same with the open-loop zero at $-I_{\mathrm{dc}}/C_{\mathrm{dc}}V_{\mathrm{dc}}$ in (2), which is eliminated together with G_d. However, the dominant pole, which is generated by the open-loop zero with the feedback control, may jeopardize the stability of the dc-link voltage control. By decreasing the active power from rectifier modes to inverter modes, the dominant pole is shifted to the right half-plane, as shown in Fig. 6. Hence, the ac-dc interactions can affect the dc-link voltage control depending on the rectifier or inverter mode. In the rectifier mode, a RHP zero is caused by the ac-dc interactions, which imposes the non-minimum-phase response to the dc-link

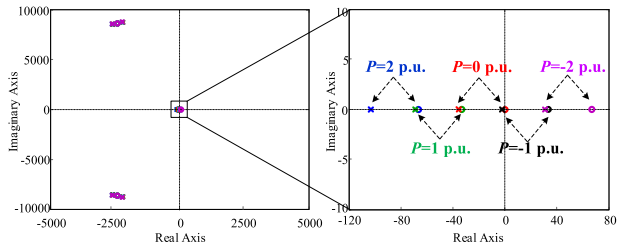

Fig. 6. Pole-zero map of the G_{cldd} with different power.

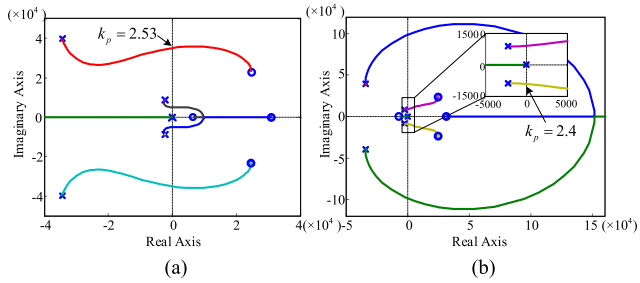

Fig. 7. Root loci of the VSC. (a). Rectifier mode. (b). Inverter mode.

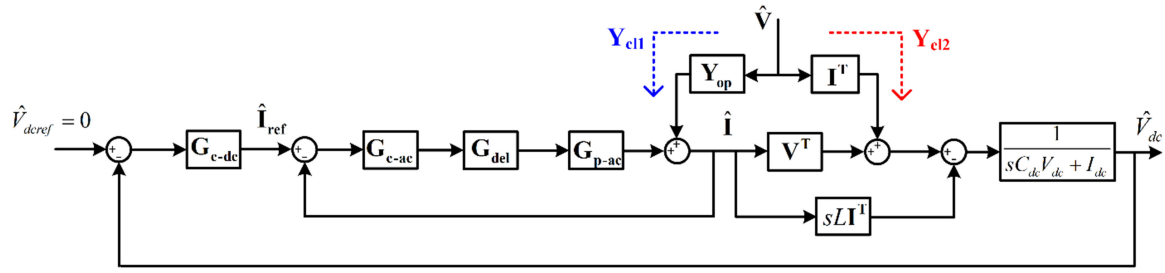

Fig. 8. Block diagram of the transfer function matrices of the VSCs with cascaded control loops.

TABLE II
CONTROL PARAMETERS

Symbol	Controller Parameter		Value
k_p	Proportional gain of dc-link voltage controllers in rectifier mode	BW=100 Hz	0.5 S
		BW=280 Hz	1.4 S
		BW=400 Hz	2 S
	Proportional gain of dc-link voltage controllers in inverter mode	BW=100 Hz	0.5 S
		BW=300 Hz	1.5 S
		BW=400 Hz	2 S
k_i	Integral gain of dc-link voltage controllers in rectifier mode	BW=100 Hz	5 S/s
		BW=280 Hz	5 S/s
		BW=400 Hz	5 S/s
	Integral gain of dc-link voltage controllers in inverter mode	BW=100 Hz	5 S/s
		BW=300 Hz	5 S/s
		BW=400 Hz	5 S/s
k_{pac}	Proportional gain of current controller		18.8 Ω
k_{iac}	Integral gain of current controller		600 Ω/s

dynamics and degrades the control performance. In contrast, in the inverter mode, the ac–dc interactions introduce a RHP pole in the case of high power operation, which imposes limitations on the dc-link voltage controller design.

B. Stability Analysis With Zero Grid Impedance

Ensuring the stability of the VSC with a zero grid impedance is necessary for using the impedance-based method to analyze the interaction between the VSC and different grid impedances [19]. Hence, prior to the impedance-based analysis, the root loci for the dc-link voltage control with zero grid impedance are plotted below, in order to analyze the dc-link dynamics with different operations modes of the VSC.

Based on (13), Fig. 7 shows the root loci of the dc-link voltage control by varying the proportional gain of the PI controller. It can be seen that the stable region of proportional gain, k_p, in the rectifier mode is $k_p < 2.53$, and is $k_p < 2.4$ in the inverter mode.

IV. IMPEDANCE-BASED STABILITY ANALYSIS OF DC-LINK CONTROL

A. Impedance Model in dq-Frame

Rearranging Figs. 2 and 3, Fig. 8 illustrates the block diagram of the transfer function matrices for the cascaded control loops in the dq-frame. The input admittance $\mathbf{Y_{cl}}$ can be divided into two parts: the first part, $\mathbf{Y_{cl1}}$, is through the inner current control loop, and the second part, $\mathbf{Y_{cl2}}$, is through the outer dc-link voltage control loop.

Due to the ac–dc interactions presented in Section II and Section III, the open-loop input admittance $\mathbf{Y_{op}}$ is no longer the same with the L-filter plant, which is given as

$$\mathbf{Y_{op}} = \begin{bmatrix} Y_{opdd} & Y_{opdq} \\ Y_{opqd} & Y_{opqq} \end{bmatrix} = \begin{bmatrix} \frac{(D_q^2 + s^2 LC_{\rm dc})}{sL(D_d^2 + D_q^2 + s^2 LC_{\rm dc} + \omega_1^2 LC_{\rm dc})} & \frac{-D_d D_q + s\omega_1 LC_{\rm dc}}{sL(D_d^2 + D_q^2 + s^2 LC_{\rm dc} + \omega_1^2 LC_{\rm dc})} \\ \frac{-D_d D_q - s\omega_1 LC_{\rm dc}}{sL(D_d^2 + D_q^2 + s^2 LC_{\rm dc} + \omega_1^2 LC_{\rm dc})} & \frac{(D_d^2 + s^2 LC_{\rm dc})}{sL(D_d^2 + D_q^2 + s^2 LC_{\rm dc} + \omega_1^2 LC_{\rm dc})} \end{bmatrix}. \quad (14)$$

In the $\mathbf{Y_{cl1}}$, the dc-link voltage control loop brings an additional feedback loop into the current control loop. The expression of the additional feedback loop gain $\mathbf{G_{Y1}}$ is

$$\mathbf{G_{Y1}} = \mathbf{G_{p-ac}} \mathbf{G_{del}} \mathbf{G_{c-ac}} \mathbf{G_{c-dc}} \mathbf{G_{ac-dc}}. \quad (15)$$

Combining with the current control loop, $\mathbf{Y_{cl1}}$ can be derived as

$$\mathbf{Y_{cl1}} = (\mathbf{I} + \mathbf{G_{Y1}} + \mathbf{G_{p-ac}} \mathbf{G_{del}} \mathbf{G_{c-ac}})^{-1} \mathbf{Y_{op}}. \quad (16)$$

In the $\mathbf{Y_{cl2}}$, the denominat or of $\mathbf{G_{ac-dc}}$ is presented in the open-loop gain $\mathbf{G_{Y2o}}$, which can be expressed as

$$\mathbf{G_{Y2o}} = \mathbf{G_{cl}} \mathbf{G_{c-dc}} \frac{1}{(sC_{\rm dc} V_{\rm dc} + I_{\rm dc})} \quad (17)$$

while the numerator of $\mathbf{G_{ac-dc}}$ becomes the feedback loop gain, which is $\mathbf{G_{Y2f}} = -sL\mathbf{I}^{\rm T} + \mathbf{V}^{\rm T}$. Hence, $\mathbf{Y_{cl2}}$ can be derived as

$$\mathbf{Y_{cl2}} = \mathbf{G_{Y2o}} (1 - \mathbf{G_{Y2f}} \mathbf{G_{Y2o}})^{-1} \mathbf{I}^{\rm T}. \quad (18)$$

By summing up (16) and (18), the total input admittance $\mathbf{Y_{cl}}$ is

$$\mathbf{Y_{cl}} = \mathbf{Y_{cl1}} + \mathbf{Y_{cl2}} = \begin{bmatrix} Y_{dd} & Y_{dq} \\ Y_{qd} & Y_{qq} \end{bmatrix}. \quad (19)$$

To investigate the impedance shaping effect of the dc-link voltage control, both the rectifier mode and the inverter mode are analyzed with three sets of dc-link voltage controller parameters. All the parameters are in the stable region (with zero grid impedance), according to the aforementioned root loci analysis shown in Fig. 7. The inner current control loop is designed with 1 kHz bandwidth (BW) based on [20], [27]. Table II provides the

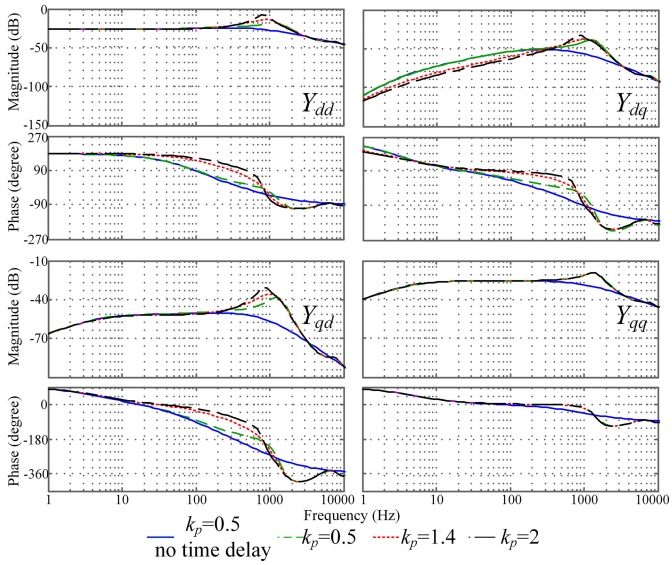

Fig. 9. Input admittance $\mathbf{Y_{cl}}$ of rectifier mode represented in the dq-frame.

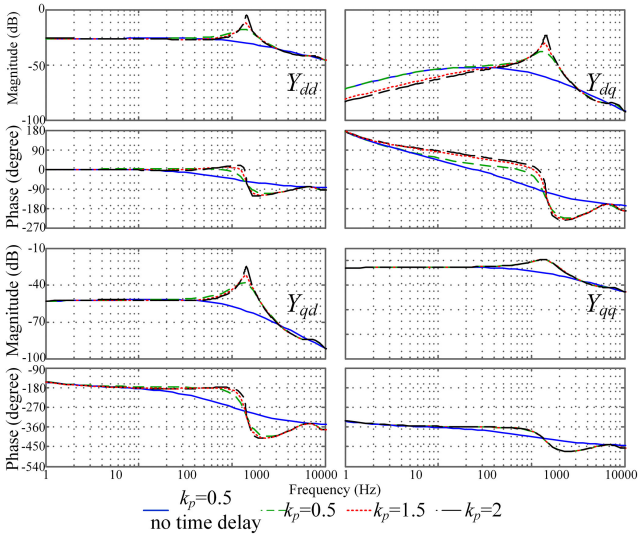

Fig. 10. Input admittance $\mathbf{Y_{cl}}$ of inverter mode represented in the dq-frame.

parameters of the dc-link voltage controllers and the ac current controller.

Fig. 9 shows the bode plot of the input admittance $\mathbf{Y_{cl}}$ of the rectifier mode. Three cases corresponding to the three sets of dc-link voltage controllers are compared. It can be observed that the negative impedance occurs merely in the low-frequency range in Y_{dd} without the digital time delay effect. When considering the digital time delay, a high-frequency range negative impedance appears. Moreover, with increasing the proportional gain k_p of the dc-link voltage controller, the range of the low-frequency negative impedance becomes wider, while the high-frequency range moves toward lower values.

Fig. 10 shows the bode plot of the input admittance $\mathbf{Y_{cl}}$ for the inverter mode, where only a high-frequency range negative impedance can be observed in Y_{dd}. Moreover, a higher proportional gain of the dc-link voltage controller leads to a wider frequency range of the negative impedance in the inverter mode. Thus, comparing the cases in the rectifier mode and that in the inverter mode, the impedance model indicates that the negative impedance in the low-frequency range is caused by the operation modes of the VSC and its control loops, while the digital time delay effect leads to an additional negative impedance in the high-frequency range. The presence of RHP zero in the rectifier mode brings a negative impedance in the low-frequency range, while the inverter mode has a positive impedance, i.e., impedance with positive real part, in the low-frequency range. Furthermore, the changes of the high-frequency range negative impedance with the variation of the controller gain are the same in the rectifier mode and inverter mode.

B. *Impedance-Based Stability Analysis in dq-Frame*

In order to assess the system stability by using the impedance-based method with the multi-input multi-output system in the dq-frame, the generalized Nyquist criterion [29] are applied to the impedance ratio $\mathbf{T}$ between the grid impedance and the inverter impedance [21], [30], which are given by

$$\mathbf{T} = \mathbf{Z_{gdq}}\mathbf{Y_{cl}} \tag{20}$$

where $\mathbf{Z_{gdq}}$ is the grid impedance matrix in the dq-frame. The overall system stability can then be predicted by the eigenvalues of the impedance ratio, which is the solution of

$$\det(\lambda\mathbf{I} - \mathbf{T}) = \det(\lambda\mathbf{I} - \mathbf{Z_{gdq}}\mathbf{Y_{cl}}) = 0 \tag{21}$$

where $\mathbf{Z_{gdq}}$ is the transfer function matrix of the LC-type grid impedance in the dq-frame.

Substituting (19) and (20) into (21), the eigenvalues can be obtained. The frequency responses of the eigenvalues are plotted to evaluate the stability of the system. According to the Nyquist criterion, the system is stable when the eigenvalues never encircle $(-1, 0)$.

First, considering the rectifier mode, the frequency responses of the eigenvalues are depicted in Fig. 11. The magnitudes of both the eigenvalues are always negative when the phase cross $-180°$, as shown in Fig. 11(a), which implies that the eigenvalues never encircle $(-1, 0)$ and the VSC system is stable. However, by increasing the proportional gain of the dc-link voltage controller, the frequency responses vary. In Fig. 11(b), when increasing k_p to 1.4, one of the eigenvalues in black remains stable while the other in red shows instability. At -274 and 274 Hz, where the phase cross $-180°$, the magnitude is 0.4 dB. This indicates that the system is unstable but quite near the stable boundary, which implies that the system diverges slowly with resonances occurring nearby 274 Hz. When k_p is increased to two, as shown in Fig. 11(c), the system turns to be unstable with encircling $(-1, 0)$, because the magnitude of the eigenvalue in red is positive with 33 dB other than near 0 dB when the phase cross $-180°$ at 300 Hz.

Then, Fig. 12 shows the frequency responses for the eigenvalues in the inverter mode. Fig. 12(a) depicts that the VSC system is kept stable with $k_p = 0.5$, because the eigenvalues never encircle $(-1, 0)$ since the magnitudes of both the eigenvalues are always negative when the phase cross $-180°$. Fig. 12(b) plots

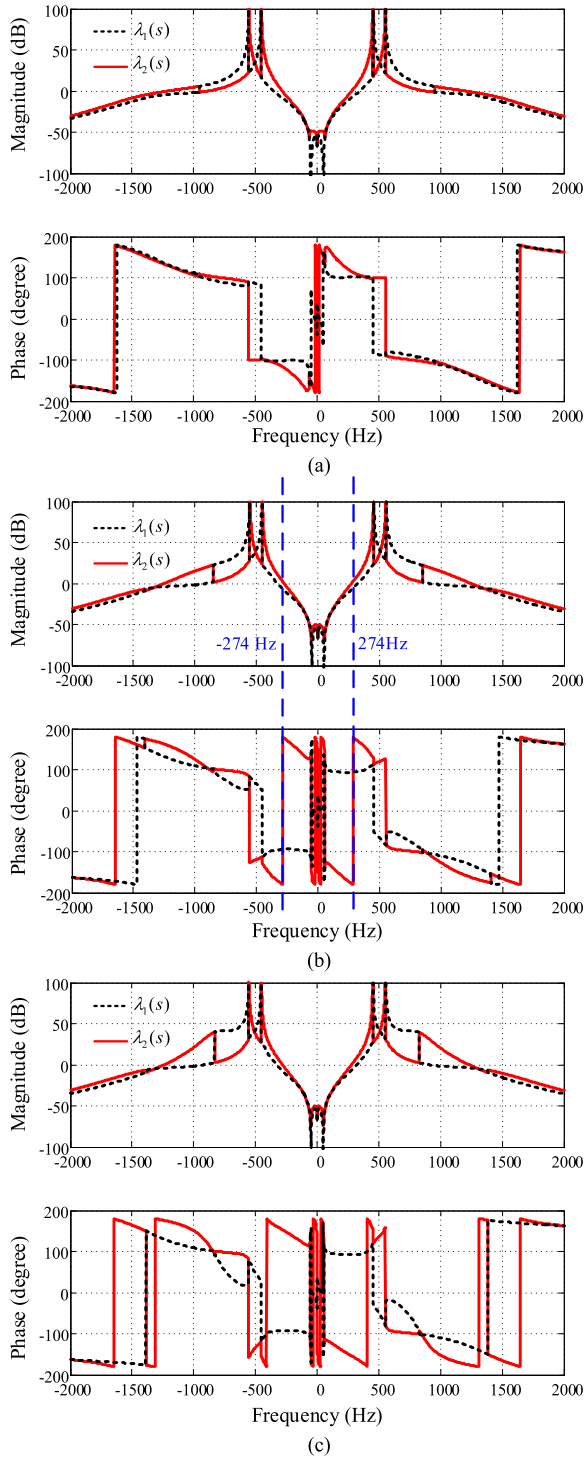

Fig. 11. Frequency response of the eigenvalues in the rectifier mode. (a) $k_p = 0.5$. (b) $k_p = 1.4$. (c) $k_p = 2.0$.

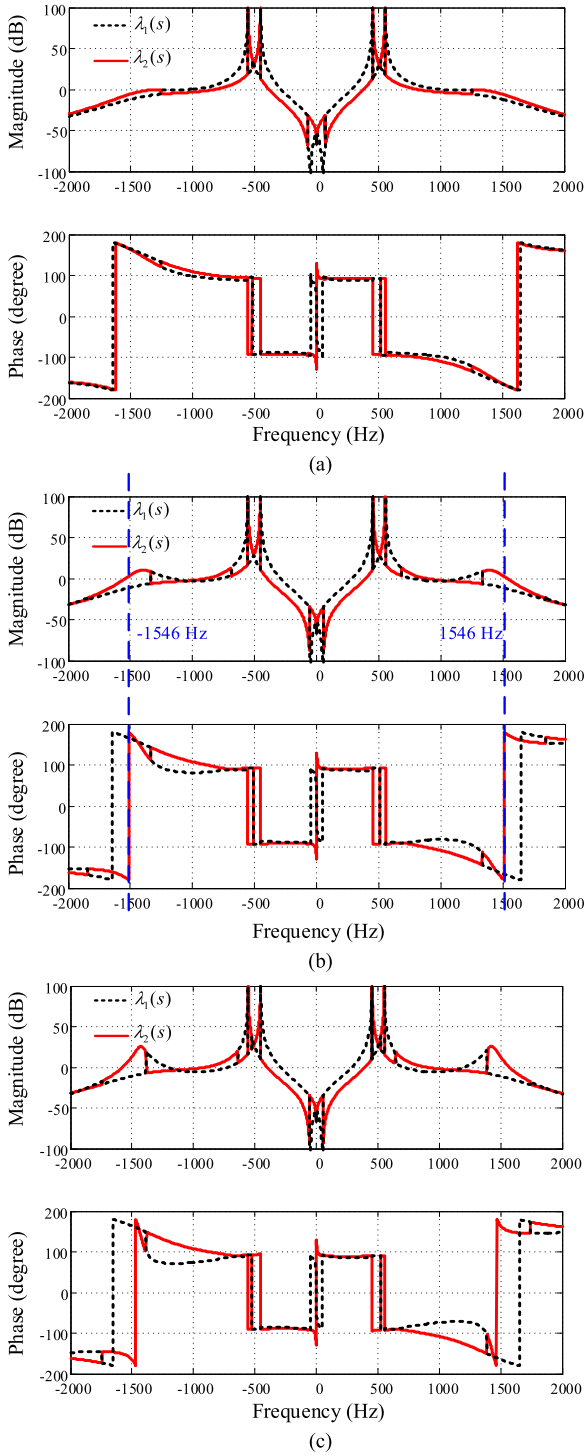

Fig. 12. Frequency response of the eigenvalues in the inverter mode. (a) $k_p = 0.5$. (b) $k_p = 1.5$. (c) $k_p = 2.0$.

the frequency responses for $k_p = 1.5$, where the magnitude is 0.6 dB at the phase crossover frequency 1546 Hz. Thus, resonant components around 1546 Hz would appear in the system performance. When increasing k_p to two, as shown in Fig. 12(c), the red eigenvalue encircle $(-1, 0)$, since the magnitude of it is 26 dB when the phase cross $-180°$ at 1480 Hz, which predicts the system is far away from the stable boundary.

C. *dq*-Frame to $\alpha\beta$-Frame

The resonant frequencies illustrated above for the rectifier and inverter mode are still in the dq-frame, which cannot reveal the real resonant frequencies at the PCC. Hence, the impedance model in the $\alpha\beta$-frame needs to be built. For the symmetric impedance matrix, i.e., $Y_{dd} = Y_{qq}, Y_{dq} = -Y_{qd}$, it is simple to transform dq-frame model to $\alpha\beta$-frame model by substituting

the s with $s - j\omega_1$ [31], [32], which is given as

$$\mathbf{Y}_{dq}(s) \Rightarrow \mathbf{Y}_{\alpha\beta}(s - j\omega_1). \tag{22}$$

However, for the dq-frame impedance model obtained in this paper, which is an asymmetric impedance matrix because of the dc-link voltage control loop, the simple frequency shift fails to build a $\alpha\beta$-frame model. To solve this problem, the complex transfer matrix is introduced. The complex transfer matrix in the dq-frame, $\mathbf{Y_{dq}}$, can be derived as follows [9], [31]:

$$\begin{aligned}\begin{bmatrix}\hat{I}_d\\ \hat{I}_q\end{bmatrix} &= \begin{bmatrix}Y_{dd}\ Y_{dd}\\ Y_{qd}\ Y_{qq}\end{bmatrix}\begin{bmatrix}\hat{V}_d\\ \hat{V}_q\end{bmatrix} \Rightarrow \begin{bmatrix}\hat{\mathbf{I}}_{\mathbf{dq}}\\ \hat{\mathbf{I}}^*_{\mathbf{dq}}\end{bmatrix}\\ &= \underbrace{\begin{bmatrix}\mathbf{Y_{dq+}}\ \mathbf{Y_{dq-}}\\ \mathbf{Y}^*_{\mathbf{dq-}}\ \mathbf{Y}^*_{\mathbf{dq+}}\end{bmatrix}}_{\mathbf{Y_{dq}}}\begin{bmatrix}\hat{\mathbf{V}}_{\mathbf{dq}}\\ \hat{\mathbf{V}}^*_{\mathbf{dq}}\end{bmatrix}\end{aligned} \tag{23}$$

$$\begin{bmatrix}\hat{\mathbf{I}}_{\mathbf{dq}}\\ \hat{\mathbf{I}}^*_{\mathbf{dq}}\end{bmatrix} = \begin{bmatrix}\hat{I}_d + j\hat{I}_q\\ \hat{I}_d - j\hat{I}_q\end{bmatrix}, \begin{bmatrix}\hat{\mathbf{V}}_{\mathbf{dq}}\\ \hat{\mathbf{V}}^*_{\mathbf{dq}}\end{bmatrix} = \begin{bmatrix}\hat{V}_d + j\hat{I}_q\\ \hat{V}_d - j\hat{I}_q\end{bmatrix} \tag{24}$$

$$\mathbf{Y_{dq+}} = \frac{Y_{dd} + Y_{qq} + j(Y_{qd} - Y_{dq})}{2} \tag{25}$$

$$\mathbf{Y_{dq-}} = \frac{Y_{dd} - Y_{qq} + j(Y_{qd} + Y_{dq})}{2} \tag{26}$$

where $\mathbf{Y}^*_{\mathbf{dq+}}$ and $\mathbf{Y}^*_{\mathbf{dq-}}$ are the complex conjugates of the $\mathbf{Y_{dq+}}$ and $\mathbf{Y_{dq-}}$.

Considering $\mathbf{Y_{dq}}$ in a fractional form given as follows:

$$\mathbf{Y_{dq}} = \begin{bmatrix}\mathbf{Y_{dq+}}\ \mathbf{Y_{dq-}}\\ \mathbf{Y}^*_{\mathbf{dq-}}\ \mathbf{Y}^*_{\mathbf{dq+}}\end{bmatrix} = \begin{bmatrix}\frac{\mathbf{M}_+(s)}{\mathbf{N}_+(s)}\ \frac{\mathbf{M}_-(s)}{\mathbf{N}_-(s)}\\ \frac{\mathbf{M}^{\mathbf{m}}_-(s)}{\mathbf{N}^{\mathbf{m}}_-(s)}\ \frac{\mathbf{M}^{\mathbf{m}}_+(s)}{\mathbf{N}^{\mathbf{m}}_+(s)}\end{bmatrix} \tag{27}$$

then, by using the frequency translation of complex transfer functions, the complex transfer matrix in the dq-frame can be transformed into the $\alpha\beta$-frame. Taking transforming $\mathbf{Y_{dq}}$ as an example, the derivation is elaborated as follow:

$$\hat{\mathbf{I}}_{\mathbf{dq}} = \mathbf{Y_{dq-}}\hat{\mathbf{V}}^*_{\mathbf{dq}} \Rightarrow \hat{\mathbf{I}}_{\mathbf{dq}} = \frac{\mathbf{M}_-(s)}{\mathbf{N}_-(s)}\hat{\mathbf{V}}^*_{\mathbf{dq}} \Rightarrow$$

$$e^{-j\theta}\hat{\mathbf{I}}_{\alpha\beta} = \frac{\mathbf{M}_-(s)}{\mathbf{N}_-(s)}e^{j\theta}\hat{\mathbf{V}}^*_{\alpha\beta} \Rightarrow$$

$$\mathbf{N}_-(s)e^{-j\theta}\hat{\mathbf{I}}_{\alpha\beta} = \mathbf{M}_-(s)e^{j\theta}\hat{\mathbf{V}}^*_{\alpha\beta} \tag{28}$$

$$\Rightarrow e^{-j\theta}\mathbf{N}_-(s - j\omega_1)\hat{\mathbf{I}}_{\alpha\beta} = e^{j\theta}\mathbf{M}_-(s + j\omega_1)\hat{\mathbf{V}}^*_{\alpha\beta} \Rightarrow$$

$$\mathbf{N}_-(s - j\omega_1)\hat{\mathbf{I}}_{\alpha\beta} = e^{j2\theta}\mathbf{M}_-(s + j\omega_1)\hat{\mathbf{V}}^*_{\alpha\beta} \Rightarrow$$

$$\mathbf{N}_-(s - j\omega_1)\hat{\mathbf{I}}_{\alpha\beta} = \mathbf{M}_-(s - j\omega_1)e^{j2\theta}\hat{\mathbf{V}}^*_{\alpha\beta} \tag{29}$$

$$\Rightarrow \hat{\mathbf{I}}_{\alpha\beta} = \frac{\mathbf{M}_-(s - j\omega_1)}{\mathbf{N}_-(s - j\omega_1)}e^{j2\theta}\hat{\mathbf{V}}^*_{\alpha\beta} \tag{30}$$

where $e^{-j\theta} = \cos(\theta) - j\sin(\theta)$ is the complex form of the Park transformation [31]. Thus, the complex transfer matrix in the $\alpha\beta$-frame can be obtained as

$$\begin{bmatrix}\hat{\mathbf{I}}_{\alpha\beta}\\ e^{j2\theta}\hat{\mathbf{I}}^*_{\alpha\beta}\end{bmatrix} = \begin{bmatrix}\frac{\mathbf{M}_+(s-j\omega_1)}{\mathbf{N}_+(s-j\omega_1)}\ \frac{\mathbf{M}_-(s-j\omega_1)}{\mathbf{N}_-(s-j\omega_1)}\\ \frac{\mathbf{M}^{\mathbf{m}}_-(s-j\omega_1)}{\mathbf{N}^{\mathbf{m}}_-(s-j\omega_1)}\ \frac{\mathbf{M}^{\mathbf{m}}_+(s-j\omega_1)}{\mathbf{N}^{\mathbf{m}}_+(s-j\omega_1)}\end{bmatrix}\begin{bmatrix}\hat{\mathbf{V}}_{\alpha\beta}\\ e^{j2\theta}\hat{\mathbf{V}}^*_{\alpha\beta}\end{bmatrix}$$

$$\Downarrow$$

$$\begin{bmatrix}\hat{\mathbf{I}}_{\alpha\beta}\\ e^{j2\theta}\hat{\mathbf{I}}^*_{\alpha\beta}\end{bmatrix} = \underbrace{\begin{bmatrix}\mathbf{Y_{dq+}}(s - j\omega_1)\ \mathbf{Y_{dq-}}(s - j\omega_1)\\ \mathbf{Y}^*_{\mathbf{dq-}}(s - j\omega_1)\ \mathbf{Y}^*_{\mathbf{dq+}}(s - j\omega_1)\end{bmatrix}}_{\mathbf{Y}_{\alpha\beta}}\begin{bmatrix}\hat{\mathbf{V}}_{\alpha\beta}\\ e^{j2\theta}\hat{\mathbf{V}}^*_{\alpha\beta}\end{bmatrix} \tag{31}$$

where $\mathbf{Y}_{\alpha\beta}$ is the complex transfer matrix in the $\alpha\beta$-frame. Compared with the dq-frame complex transfer matrix in (23) and (27), substituting s with $s - j\omega_1$ can still be established for transforming the dq-frame model to the $\alpha\beta$-frame model. However, the input and output in the $\alpha\beta$-frame model are $[\,\hat{\mathbf{V}}_{\alpha\beta}\ e^{j2\theta}\hat{\mathbf{V}}^*_{\alpha\beta}\,]^{\mathrm{T}}$ and $[\,\hat{\mathbf{I}}_{\alpha\beta}\ e^{j2\theta}\hat{\mathbf{I}}^*_{\alpha\beta}\,]^{\mathrm{T}}$, other than $[\,\hat{\mathbf{V}}_{\alpha\beta}\ \hat{\mathbf{V}}^*_{\alpha\beta}\,]^{\mathrm{T}}$ and $[\,\hat{\mathbf{I}}_{\alpha\beta}\ \hat{\mathbf{I}}^*_{\alpha\beta}\,]^{\mathrm{T}}$.

With the rotating factor $e^{j2\theta}$ existing in the input and output, the impedance model (31) can be regarded as a double frequency model and the difference between the two frequencies is $2\omega_1$. Additionally, since the nondiagonal elements in the complex transfer matrix (31) are not zero, which indicates this double frequency model has couplings between the two frequencies. Thus, for a given vector at the frequency ω, a frequency-coupled vector at $2\omega_1 - \omega$ is yielded from (31). When the frequency is above ω, the coupled frequency $2\omega_1 - \omega$ is negative, which demonstrates the couplings between the positive and negative sequence components. Otherwise, when the frequency is below ω_1, the couplings occur between the two positive sequence components, since $2\omega_1 - \omega$ is a positive frequency.

Applying the impedance-based stability analysis, the impedance ratio in the $\alpha\beta$-frame, $\mathbf{T}_{\alpha\beta}$, is

$$\mathbf{T}_{\alpha\beta} = \mathbf{Z_{g}}_{\alpha\beta}\mathbf{Y_{cl}}_{\alpha\beta} \tag{32}$$

where $\mathbf{Z_{g}}_{\alpha\beta}$ and $\mathbf{Y_{cl}}_{\alpha\beta}$ are the grid impedance and input admittance of the VSC in the $\alpha\beta$-frame, which can be derived by following (23)–(31).

Although the single frequency oscillation predicted by the impedance model in the dq-frame model can be easily transferred to two frequencies in abc or $\alpha\beta$-frame with the frequency shift [31], [32], the dq-frame model fails to analyze the coupling effect between these two frequencies, since the coupling between d- and q-axes reveal nothing in the frequency domain. Hence, the impedance model in $\alpha\beta$-frame, a double-frequency model with 100 Hz difference, which can clearly reveal that these two frequencies are coupled with each other due to the coupling terms.

V. Simulation and Experimental Results

A. Simulation Results

To verify the impedance model and stability analysis of the dc-link voltage control in the VSC, the time domain simulations

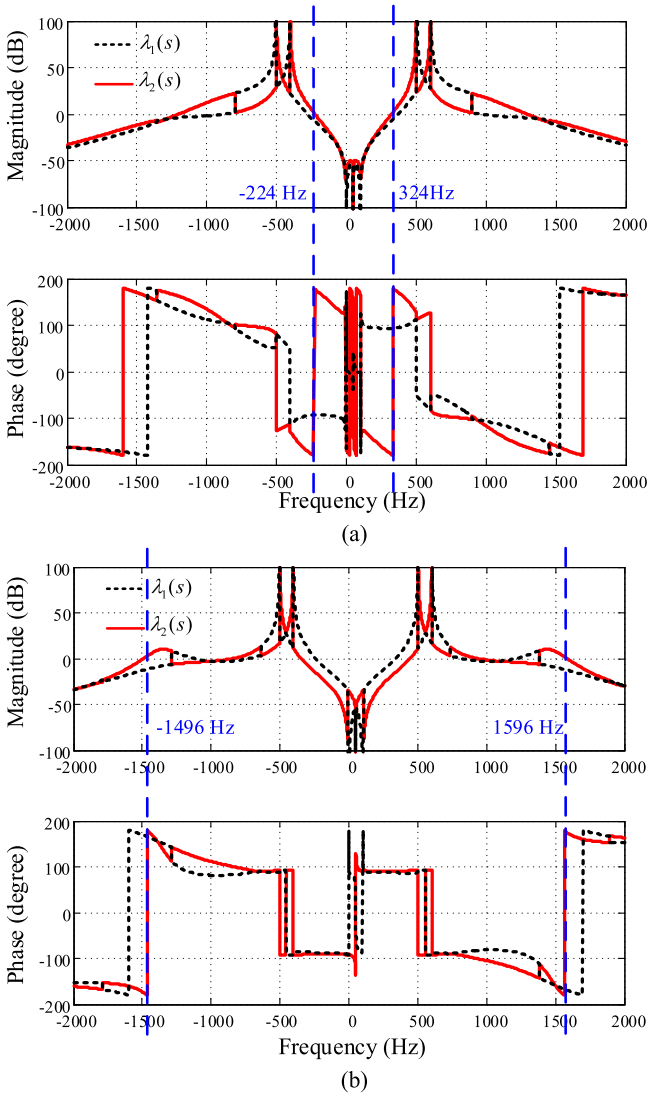

Fig. 13. Frequency response of the eigenvalues in the $\alpha\beta$-frame. (a) Rectifier mode, $k_p = 1.4$. (b) Inverter mode, $k_p = 1.5$.

carried out in MATLAB/SIMULINK and PLECS Blockset are presented. The parameters listed in Table I and Table II are adopted.

Fig. 14 shows the simulated waveforms of the PCC voltage (phase voltage $V_i, i = A, B, C$), input current ($I_i, i = A, B, C$), and dc-link voltage ($V_{\rm dc}$) for the VSC in the rectifier mode. It can be seen in Fig. 14(a) that the system is stable when $k_p = 0.5$, which is consistent with the frequency domain analysis in Fig. 11(a). Compared with Fig. 11(b), harmonic oscillations occur in case of $k_p = 1.4$. To further confirm the stability prediction, Fig. 15 illustrates the harmonic spectrum of the Fig. 14(b), where two main harmonic components close to the frequencies identified in Fig. 13(a) can be observed. The two frequencies shift compared with the one identified in Fig. 11(b) verify the frequency-coupling effect caused by dc-link voltage control. Fig. 14(c) shows the system response by changing k_p from 0.5 to 2 at 2.44 s, where the VSC system turns to be unstable.

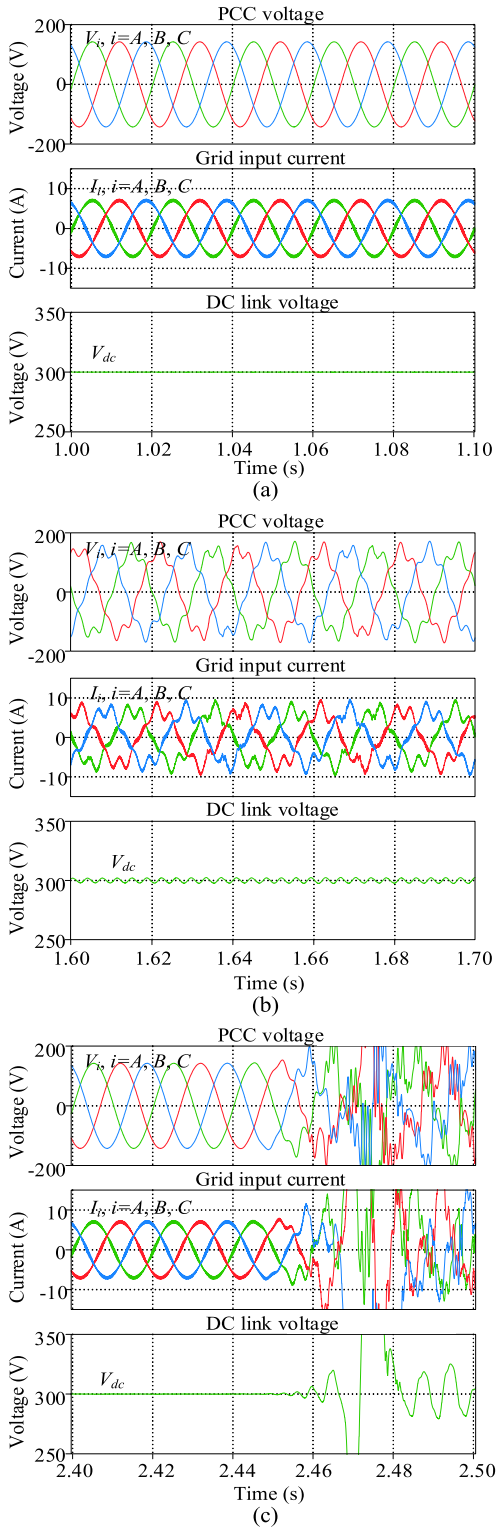

Fig. 14. Simulated waveforms of VSC in the rectifier mode. (a) $k_p = 0.5$. (b) $k_p = 1.4$. (c) $k_p = 2.0$.

Fig. 16 shows the simulated results for the VSC in the inverter mode. Stable waveforms can be observed in Fig. 16(a). When increasing the dc controller gain to 1.5, as implicated in the frequency analysis in Fig. 12(b), oscillations can be seen in Fig. 16(b). Fig. 17 gives the harmonic spectra results, where two

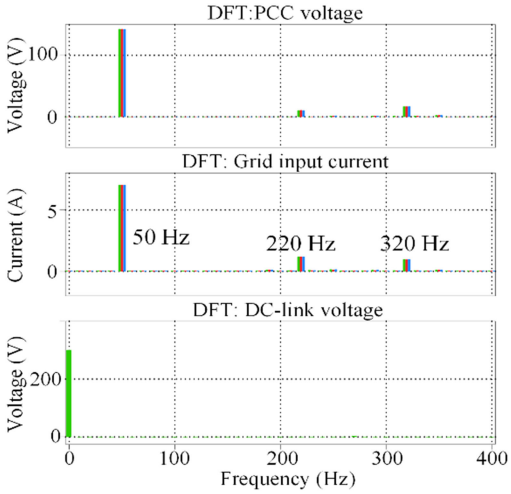

Fig. 15. Harmonic spectrum of the simulated waveforms in Fig. 14(b).

high frequencies are obtained, which are correlated to the ones presented in Fig. 13(b). Combining the results in the rectifier mode, it is clear that the dc-link voltage control can introduce low-frequency distortions in the rectifier mode other than high-frequency distortions in the inverter mode. Fig. 15(c) shows that the system becomes unstable after increasing k_p from 1.5 to 2 at 3.53 s.

B. Experimental Results

In order to verify the stability analysis, a test setup of the three phase VSC is built as shown in Fig. 18, where a Chroma grid simulator is used for generating grid voltage, a Danfoss frequency converter is used as the VSC including the dc-link and a Cinergia electronic load is used as the dc-link current source. The control system is implemented in the DS1007 dSPACE system. The parameters used in the experiments are the same with the simulation analysis.

Fig. 19 shows the measured waveforms of the PCC voltage (line to line, V_{AB}), phase A input current (I_A), and dc-link voltage ($V_{\rm dc}$) for the VSC in the rectifier mode. Two sets of the dc controller, i.e., $k_p = 0.5$ and $k_p = 1.4$, are tested, since the system is tripping in case of $k_p = 2$. In Fig. 19(a), the system is stable with $k_p = 0.5$, which agrees with the simulation results in Fig. 14(a). When increasing k_p to 1.4, the voltages and current are distorted as shown in Fig. 19(b). The DFT analysis of phase A current shows two main resonant components at 220 and 320 Hz, which match the resonant frequencies analysis in Fig. 13(a) and Fig 15.

Fig. 20 shows the measured waveforms of PCC voltage (line to line, V_{AB}), phase A input current (I_A), and dc-link voltage ($V_{\rm dc}$) for the VSC in the inverter mode. Similarly, $k_p = 2$ trips the system due to the instability, where the protection circuit acts as the voltages and currents diverge quickly. Thus, the cases of $k_p = 0.5$ and $k_p = 1.4$ are presented. It can be seen that the system is stable with $k_p = 0.5$ in Fig. 20(a) and high-frequency oscillations occur with $k_p = 1.5$ in Fig. 20(b). The frequencies shown in the DFT analysis of phase A current are 1500 and 1600 Hz, which are close to the

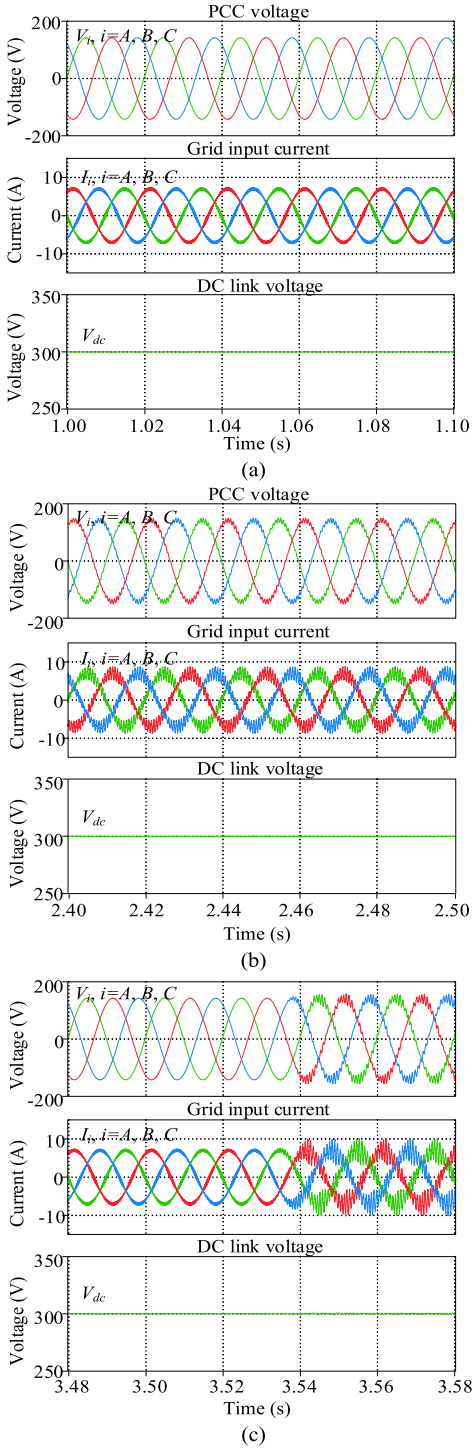

Fig. 16. Simulated waveforms of VSC in the inverter mode. (a) $k_p = 0.5$. (b) $k_p = 1.5$. (c) $k_p = 2.0$.

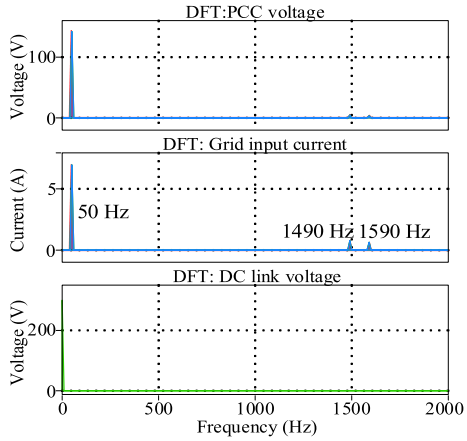

Fig. 17. Harmonic spectrum of the simulated waveforms in Fig. 16(b).

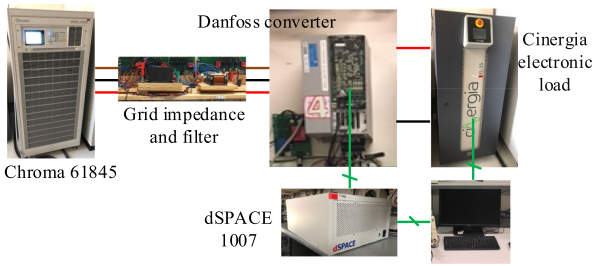

Fig. 18. Experimental setup in the lab.

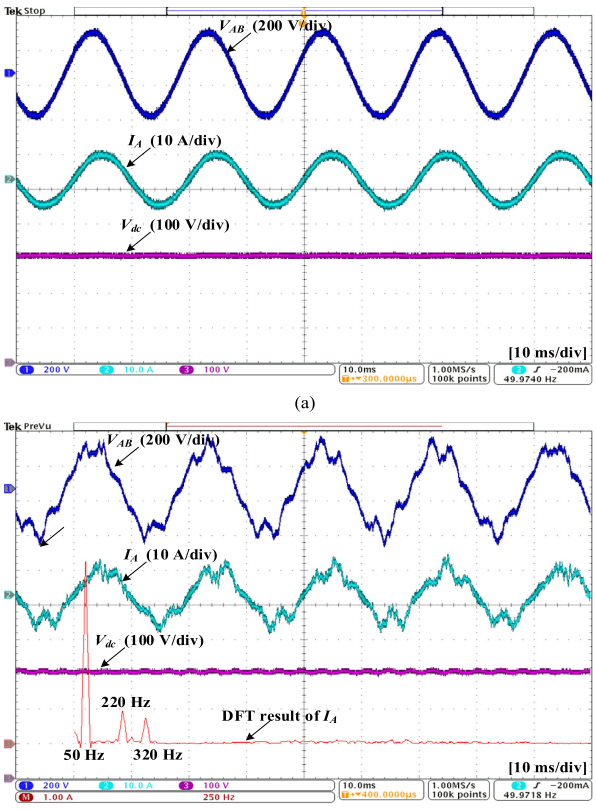

Fig. 19. Experimental waveforms of the PCC voltage, input current and dc-link voltage in the rectifier mode. (a) $k_p = 0.5$. (b) $k_p = 1.4$.

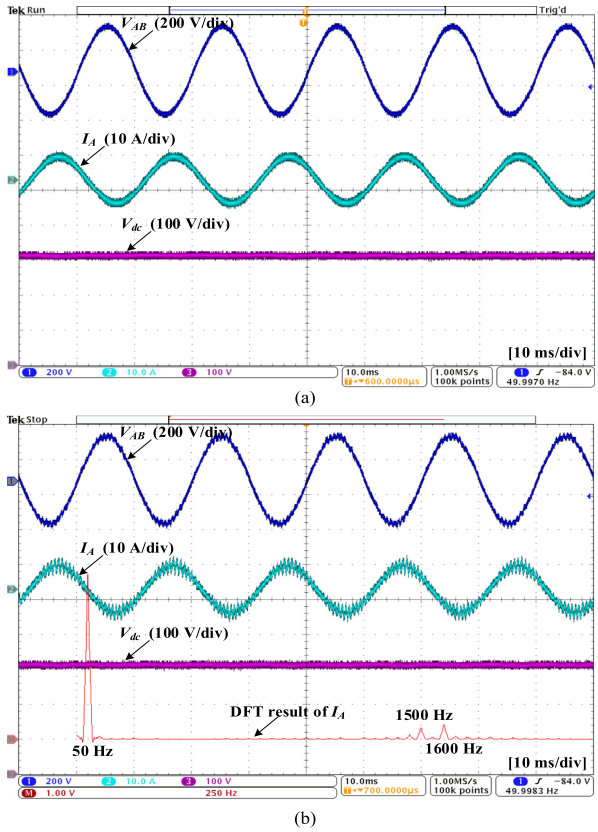

Fig. 20. Experimental waveforms of the PCC voltage, input current and dc-link voltage in the inverter mode. (a) $k_p = 0.5$. (b) $k_p = 1.5$.

eigenvalue analysis shown in Fig. 13(b) and the simulation results in Fig. 17.

VI. Conclusion

This paper presents the stability analysis of dc-link voltage control in VSC based on the impedance method. A stability-oriented model is derived with a full order small-signal model and the ac–dc interactions are discussed. The dc-link dynamics can affect the inner ac current control plant in terms of operation conditions. Based on that, the impact of the VSC parameters on the stability of the dc-link voltage control is carried out, where the critical value of the dc-link voltage controller gain varies from the rectifier mode to the inverter mode. Impedance models in both dq-frame and $\alpha\beta$-frame have been developed. The relationship between the dq-frame and $\alpha\beta$-frame model are explicitly revealed with a complex transfer matrix. The frequency-coupling effect resulted by the dc-link voltage control has been discussed based on the impedance model. Eigenvalue analysis on the influence of different dc-link controller has been performed with the impedance model, which indicates that the dc-link control voltage leads to low-frequency oscillations in the rectifier mode and high-frequency oscillations in the inverter mode. Simulations and experiments validate the impedance model and stability analysis.

REFERENCES

[1] F. Blaabjerg, Z. Chen, and S. B. Kjaer, "Power electronics as efficient interface in dispersed power generation systems," *IEEE Trans. Power Electron.*, vol. 19, no. 5, pp. 1184–1194, Sep. 2004.

[2] J. Rocabert, A. Luna, F. Blaabjerg, and P. Rodriguez, "Control of power converters in ac microgrids," *IEEE Trans. Power Electron.*, vol. 27, no. 11, pp. 4734–4749, Nov. 2012.

[3] L. Harnefors, X. Wang, A. G. Yepes, and F. Blaabjerg, "Passivity-Based stability assessment of grid-connected VSCs—an overview," *IEEE J. Emerg. Sel. Top. Power Electron.*, vol. 4, no. 1, pp. 116–125, Mar. 2016.

[4] X. Wang, F. Blaabjerg, and W. Wu, "Modeling and analysis of harmonic Stability in an ac power-electronics-based power system," *IEEE Trans. Power Electron.*, vol. 29, no. 12, pp. 6421–6432, Dec. 2014.

[5] H. Bai, X. Wang, and F. Blaabjerg, "Passivity enhancement in renewable energy source based power plant with Paralleled grid-connected VSIs, " *IEEE Trans. Ind. Appl.*, vol. 53, no. 4, pp. 3793–3802, Jul./Aug. 2017.

[6] X. Wang, F. Blaabjerg, M. Liserre, Z. Chen, J. He, and Y. Li, "An active damper for stabilizing power-electronics-based AC systems," *IEEE Trans. Power Electron.*, vol. 29, no. 7, pp. 3318–3329, Jul. 2014.

[7] B. Wen, D. Boroyevich, R. Burgos, P. Mattavelli, and Z. Shen, "Analysis of D-Q small-signal impedance of grid-tied inverters, " *IEEE Trans. Power Electron.*, vol. 31, no. 1, pp. 675–687, Jan. 2016.

[8] M. K. Bakhshizadeh, X. Wang, F. Blaabjerg, L. Kocewiak, C. L. Bak, and B. Hesselbak, "Couplings in phase domain impedance modelling of grid-connected converters," *IEEE Trans. Power Electron.*, vol. 31, no. 10, pp. 6792–6796, Oct. 2016.

[9] X. Wang, L. Harnefors, and F. Blaabjerg, "Unified impedance model of grid-connected voltage-source converters," *IEEE Trans. Power Electron.*, vol. 33, no. 2, pp. 1775–1787, Feb. 2018.

[10] K. D. T. Ngo, "Low-frequency Characterization of PWM Converters," *IEEE Trans. Power Electron.*, vol. PE-1, no. 4, pp. 223–230, Oct. 1986.

[11] S. Hiti, D. Boroyevich, and C. Cuadros, "Small-signal modeling and control of three-phase PWM converters," in *Proc. Ind. Appl. Soc. Annu. Meet.*, Oct. 1994, vol. 2, pp. 1143–1150.

[12] S. Hiti, V. Vlatkovic, D. Borojevic, and F. C. Lee, "A new control algorithm for three-phase PWM buck rectifier with input displacement factor compensation," *IEEE Trans. Power Electron.*, vol. 9, no. 2, pp. 173–180, Mar. 1994.

[13] V. Blasko and V. Kaura, "A new mathematical model and control of a three-phase AC-DC voltage source converter," *IEEE Trans. Power Electron.*, vol. 12, no. 1, pp. 116–123, Jan. 1997.

[14] H. Mao, D. Boroyevich, and F. C. Y. Lee, "Novel reduced-order small-signal model of a three-phase PWM rectifier and its application in control design and system analysis," *IEEE Trans. Power Electron.*, vol. 13, no. 3, pp. 511–521, May 1998.

[15] B. Yin, R. Oruganti, S. K. Panda, and A. K. S. Bhat, "A simple single-input–single-output (SISO) model for a three-phase PWM rectifier," *IEEE Trans. Power Electron.*, vol. 24, no. 3, pp. 620–631, Mar. 2009.

[16] Y. Huang, X. Yuan, J. Hu, and P. Zhou, "Modeling of VSC connected to weak grid for stability analysis of DC-link voltage control," *IEEE J. Emerg. Sel. Top. Power Electron.*, vol. 3, no. 4, pp. 1193–1204, Dec. 2015.

[17] H. Yuan, X. Yuan, and J. Hu, "Modeling of grid-connected VSCs for power system small-signal stability analysis in DC-link voltage control timescale," *IEEE Trans. Power Syst.*, vol. 32, no. 5, pp. 3981–3991, Sep. 2017.

[18] R. D. Middlebrook, "Input filter considerations in design and application of switching regulators," in *Proc. IEEE Ind. Appl. Soc. Conf.*, Oct. 1976, pp. 94–107.

[19] J. Sun, "Impedance-based stability criterion for grid-connected inverters," *IEEE Trans. Power Electron.*, vol. 26, no. 11, pp. 3075–3078, Nov. 2011.

[20] L. Harnefors, M. Bongiorno, and S. Lundberg, "Input-admittance calculation and shaping for controlled voltage-source converters," *IEEE Trans. Ind. Electron.*, vol. 54, no. 6, pp. 3323–3334, Dec. 2007.

[21] B. Wen, D. Boroyevich, R. Burgos, P. Mattavelli, and Z. Shen, "Small-Signal stability analysis of three-Phase AC systems in the presence of constant power loads based on measured d-q frame impedances," *IEEE Trans. Power Electron.*, vol. 30, no. 10, pp. 5952–5963, Oct. 2015.

[22] M. Cespedes and J. Sun, "Impedance modeling and analysis of grid-connected voltage-source converters," *IEEE Trans. Power Electron.*, vol. 29, no. 3, pp. 1254–1261, Mar. 2014.

[23] B. Wen, D. Dong, D. Boroyevich, R. Burgos, P. Mattavelli, and Z. Shen, "Impedance-based analysis of grid-synchronization stability for three-phase paralleled converters," *IEEE Trans. Power Electron.*, vol. 31, no. 1, pp. 26–38, Jan. 2016.

[24] N. Bottrell, M. Prodanovic, and T. C. Green, "Dynamic stability of a microgrid with an active load," *IEEE Trans. Power Electron.*, vol. 28, no. 11, pp. 5107–5119, Nov. 2013.

[25] A. Yazdani and R. Iravani, "An accurate model for the DC-side voltage control of the neutral point diode clamped converter," *IEEE Trans. Power Del.*, vol. 21, no. 1, pp. 185–193, Jan. 2006.

[26] T. Messo, A. Aapro, and T. Suntio, "Generalized multivariable small-signal model of three-phase grid-connected inverter in DQ-domain," in *Proc. IEEE 16th Workshop Control Model. Power Electron.*, 2015, pp. 1–8.

[27] R. Teodorescu, M. Liserre, and P. Rodriguez, *Grid Converters for Photovoltaic and Wind Power Systems*. Piscataway, NJ, USA: Wiley-IEEE Press 2011.

[28] S. Buso and P. Mattavelli, *Digital Control in Power Electronics*. San Francisco, CA, USA: Morgan & Claypool Publ., 2006.

[29] C. Desoer and Yung-Terng Wang, "On the generalized nyquist stability criterion," *IEEE Trans. Autom. Control*, vol. 25, no. 2, pp. 187–196, Apr. 1980.

[30] M. Belkhayat, *Stability Criteria for AC Power Systems with Regulated Loads*. Ph.D. Dissertation, Purdue University, West Lafayette, Indiana, USA, Dec. 1997.

[31] L. Harnefors, "Modeling of three-phase dynamic systems using complex transfer functions and transfer matrices," *IEEE Trans. Ind. Electron.*, vol. 54, no. 4, pp. 2239–2248, Aug. 2007.

[32] J. Shen, S. Schröder, H. Stagge, and R. W. De Doncker, "Precise modeling and analysis of DQ-frame current controller for high power converters with low pulse ratio," in *Proc. Energy Convers. Congr. Expo.*, 2012, pp. 61–68.

Dapeng Lu (S'16) received the B.S. and M.S. degrees in electrical engineering from Xi'an Jiaotong University, Xi'an, China, in 2012 and 2015, respectively. He is currently working toward the Ph.D degree at the Department of Energy Technology, Aalborg University, Aalborg, Denmark.

In 2018, he was a Visiting Scholar with the Royal Melbourne Institute of Technology, Australia. His current research interests include power quality, modeling and control of grid-connected converters.

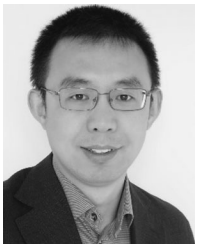

Xiongfei Wang (S'10–M'13–SM'17) received the B.S. degree from the Yanshan University, Qinhuangdao, China, in 2006, the M.S. degree from the Harbin Institute of Technology, Harbin, China, in 2008, both in electrical engineering, and the Ph.D. degree in energy technology from Aalborg University, Aalborg, Denmark, in 2013.

Since 2009, he has been with the Aalborg University, Aalborg, Denmark, where he is currently an Associate Professor with the Department of Energy Technology. His research interests include modeling and control of grid-connected converters, harmonics analysis and control, passive and active filters, stability of power electronic based power systems.

Dr. Wang was an Associate Editor for the IEEE TRANSACTIONS ON POWER ELECTRONICS, the IEEE TRANSACTIONS ON INDUSTRY APPLICATIONS, and the IEEE JOURNAL OF EMERGING AND SELECTED TOPICS IN POWER ELECTRONICS. He is also the Guest Editor for the Special Issue "Grid-Connected Power Electronics Systems: Stability, Power Quality, and Protection" in the IEEE TRANSACTIONS ON INDUSTRY APPLICATIONS. He received the second prize paper award and the Outstanding Reviewer Award of IEEE TRANSACTIONS ON POWER ELECTRONICS in 2014 and 2017, respectively, the Second Prize Paper Award of IEEE TRANSACTIONS ON INDUSTRY APPLICATIONS in 2017, and the Best Paper Awards at IEEE PEDG 2016 and IEEE PES GM 2017. In 2018, he received the IEEE PELS Richard M. Bass Outstanding Young Power Electronics Engineer Award.

Frede Blaabjerg (S'86–M'88–SM'97–F'03) received the Ph.D. degree in electrical engineering from Aalborg University, Aalborg, Denmark, in 1995.

He was with ABB-Scandia, Randers, Denmark, from 1987 to 1988. He became an Assistant Professor in 1992, an Associate Professor in 1996, and a Full Professor of power electronics and drives in 1998. From 2017, he became a Villum Investigator. He is honoris causa at University Politehnica Timisoara (UPT), Romania and Tallinn Technical University (TTU) in Estonia. His current research interests include power electronics and its applications such as in wind turbines, PV systems, reliability, harmonics, and adjustable speed drives. He has authored and coauthored more than 500 journal papers in the fields of power electronics and its applications. He is the co-author of two monographs and editor of 7 books in power electronics and its applications.

Dr. Blaabjerg was the recipient of the 26 IEEE Prize Paper Awards, the IEEE PELS Distinguished Service Award in 2009, the EPE-PEMC Council Award in 2010, the IEEE William E. Newell Power Electronics Award 2014, and the Villum Kann Rasmussen Research Award 2014. He was the Editor-in-Chief of the IEEE TRANSACTIONS ON POWER ELECTRONICS from 2006 to 2012. He has been Distinguished Lecturer for the IEEE Power Electronics Society from 2005 to 2007 and for the IEEE Industry Applications Society from 2010 to 2011 as well as 2017 to 2018. In 2018, he is President Elect of IEEE Power Electronics Society. He is nominated in 2014, 2015, 2016 and 2017 by Thomson Reuters to be among the Most 250 Cited Researchers in Engineering in the World.